Proof-of-Concept Real-Time Implementation of Interleavers for Optical Satellite Links

Daniel Romero Arrieta, Sylvain Almonacil, Jean-Marc Conan, Laurie Paillier, Eric Dutisseuil, Sébastien Bigo, Jérémie Renaudier, Rajiv Boddeda

Proof-of-Concept Real-Time Implementation of Interleavers for Optical Satellite Links

Daniel Romero Arrieta, Sylvain Almonacil, *Member, IEEE*, Jean-Marc Conan, Laurie Paillier, Eric Dutisseuil, Sébastien Bigo, *Fellow, IEEE*, Jérémie Renaudier, *Senior Member, IEEE*, and Rajiv Boddeda, *Member, IEEE*

***Abstract*—Ground-satellite optical links are a promising technology for increasing capacity and security over radio frequency links, while reducing weight and power consumption. However, atmospheric turbulence generates power fadings at the reception terminal. This effect can be mitigated by combining adaptive optics, forward error correction and data interleaving. While adaptive optics has been extensively studied, forward error correction together with long interleaving (e.g., multiple 10 ms) has not yet been demonstrated in this context. In this article, we present a proof of concept of an optical satellite uplink, pre-compensated by adaptive optics, which leverages a long interleaver in an external memory and operates at 10 Gbps with SFP+ transceivers. We account for the issues associated with real-time implementation and interfacing to a high-speed memory. To validate our proof of concept, we generate time-series for a typical ground to geostationary satellite communication link, using a field-validated simulator. Using these time series, we calculate the required interleaver time as a function of the launch power. Finally, we show the impact of different transmitter pupil diameters and of different wind speed profiles, on the interleaver duration.**

***Index Terms*—Adaptive optics, DVB-S2, FEC, FPGA, free-space optics, interleaver, satellite communications.**

I. Introduction

THE continuous increase in the demand for data transmission has pushed the state-of-the-art of radio frequency ground-satellite links to their theoretical ceiling. Optical links can bring a large capacity leap, but new challenges arise because of the specific nature of the propagation channel i.e., the atmosphere, as it induces propagation effects unknown in terrestrial fiber systems. These effects can be either static or dynamic. Some of the static effects are cloud attenuation, aerosol scattering and gas absorption [1], [2]. While the capacity can be maximized by wavelength division multiplexing channels, gas absorption attenuates the signal power by several dBs at specific wavelengths and thus limits the achievable capacity in some spectral regions. This limitation can be overcome by the optimization of wavelength allocation plans and digital signal processing techniques [3]. On the other hand, dynamic variations of the air refractive index impact the optical power on the receiver telescope. The present article concentrates on this latter effect that induces time-distributed and relatively long (few ms) attenuation peaks of received optical power (ROP). These attenuation peaks could be partially mitigated by an adaptive optics (AO) system but cannot be completely eliminated. The remaining peaks will generate long error bursts, which have been mitigated by complementary techniques.

Among them, time-diversity techniques [4], could partially alleviate the bursts, but at the expense of duplicating the communication hardware. Here we study a more promising approach to achieve error-free transmissions and decrease the launch power requirements. We complement the AO system by channel encoding and data interleaving [5]. Forward error correction (FEC) mechanisms allow us to recover randomly distributed bit errors, by segmenting data into codewords and adding redundancy. Nevertheless, the slow dynamics of the atmosphere generates long error bursts, which could be several hundreds of times longer than the forward error correction codeword length. A known solution against error bursts is to complement the FEC with data interleaving [6], [7], which allows to distribute the errors over time thereby mimicking randomly distributed errors. However, this solution requires storing data for the interleaving duration, and therefore high-end memory with sufficient capacity and data transfer speed. While state-of-the-art systems carry up to 10 Gbps data [8], future communication systems equipped with digital coherent optics will achieve capacities above 100 Gbps, where memories with even larger storage capacity and higher bandwidth are needed, making unrealistic their integration in the same integrated circuit as the coherent digital signal processor. Therefore, the memories should preferably sit next to the processor, with new challenges in interfacing.

In this article we present a proof of concept of a communication chain suitable for an optical satellite uplink pre-compensated by AO and based on FEC complemented by an interleaver implemented in an external DDR memory. We address the dimensioning of a block interleaver, accounting for

Manuscript received 15 November 2022; revised 20 January 2023 and 15 March 2023; accepted 13 April 2023. Date of publication 2 May 2023; date of current version 27 June 2023. *(Corresponding author: Daniel Romero Arrieta.)*

Daniel Romero Arrieta is with the Nokia Bell Labs, 91300 Massy, France, and also with the ONERA, DOTA, Paris Saclay University, F-92322 Paris, France (e-mail: daracone4@gmail.com).

Sylvain Almonacil, Eric Dutisseuil, Sébastien Bigo, Jérémie Renaudier, and Rajiv Boddeda are with the Nokia Bell Labs, 91300 Massy, France (e-mail: sylvain.almonacil@nokia-bell-labs.com; eric.dutisseuil@nokia-bell-labs.com; sebastien.bigo@nokia-bell-labs.com; jeremie.renaudier@nokia-bell-labs.com; rajiv.boddeda@nokia-bell-labs.com).

Jean-Marc Conan and Laurie Paillier are with the ONERA, DOTA, Paris Saclay University, F-92322 Paris, France (e-mail: jean-marc.conan@onera.fr; laurie.paillier@onera.fr).

Color versions of one or more figures in this article are available at https://doi.org/10.1109/JLT.2023.3270769.

the issues associated with interfacing and real-time implementation, i.e., the insertion of headers for deinterleaver synchronization, the coding of these headers, the required segmentation of data into blocks when moving them in/out of the external memory and the limited bandwidth of the memory [9]. We then report on the interdependence between the pupil diameter of the transmitter telescope, the FEC coding/decoding performance and the interleaver duration before discussing how to jointly optimize these parameters.

Early simulations of a 100 Mbps transmission estimated the size of a convolutional interleaver and presented the codeword error rate for different interleaver duration [10]. In [11] different types of FEC for optical satellite applications are studied and a block interleaver up to 10 ms is simulated. Nevertheless, these simulations assume bit by bit interleaving, which is not feasible in high data rate applications, due to limitations of the memory technologies which the interleaver is based on. In [12], an alternative cross-layer interleaving is proposed and simulated to decrease the memory requirements for the physical layer, also the packet error rate as a function of the interleaver duration is presented. Another publication [13] extends the research presented in [11] by simulating the different FEC types in a hardware description software. These publications simulate the interleaver by averaging the mutual information along a window of a given duration, assuming that the interleaver performs the task of ideally redistributing errors in a random way, whereas a true interleaver is blind to the position of the errors, hence a uniform distribution of errors is not always achieved.

While a characterization of the statistical distribution of the mean value and variance of the ROP, or of the bit error rate (BER) allows a qualitative comparison of the transmission performance [14], [15], a comprehensive temporal statistic of the dynamics and duration of the power fades is necessary to accurately dimension the FEC and the interleaver. Several studies have addressed this issue for downlink direction [16], [17]. Whilst a model for calculating uplink fading statistics without adaptive optics is presented in [18], the statistics with pre-compensating AO have not yet been provided to the best of the authors' knowledge. Therefore, we propose a new metric to study ROP time series based on the required interleaver time to get error-free transmissions.

The remainder of the paper is organized as follows. In Section II, we explain how we generate several ROP time series by a split-step based tool and present three different scenarios with different wind speeds to represent diverse set of atmospheric conditions. In Section III, we propose a method for calculating a block interleaver, based on the generated time-series, the FEC parameters and accounting for the different limitations arising with hardware implementation. Then, we define the interleaver time as a metric to study ROP time series, and we compare it with the fading time and interfading time metrics. In Section IV, we present the real-time implementation and, we measure the required interleaver time to obtain error-free transmissions and compare it with the calculations obtained by the proposed method. We then calculate the required interleaver time as a function of the launch power. Finally, in Section V, we study the impact of different transmission pupil diameters on the interleaver duration. Also, we show how the speed of high-altitude winds impacts the interleaver duration.

II. Atmospheric Channel Modeling

The communication chain of a free space optical link involves multiple components and parameters which, if optimized based just on static parameters such as the link distance, the required data rate per wavelength, etc., fail to provide optimal design in the presence of varying atmospheric conditions. For example, increasing the transmitter pupil diameter decreases the divergence of the optical beam. Consequently, it leads to more optical power on the receiver telescope. Mean power considerations are however not sufficient in the presence of atmospheric turbulence. Simulations have shown [19] that the performance comparison for various emission pupil diameter requires to consider the overall power statistics, since an increase of the diameter often means, for the uplink, a significant increase of the ROP variance. The turbulence strength and wind speed also influence the statistical distribution, duration, and depth of the attenuation peaks, and therefore need to be accounted for when defining the best combination of forward error correction (FEC) (type, code rate), interleaver duration, AO parameters and optical launch power.

In this section we explain how we obtain representative time series of the power coupled into the satellite receiver fiber, which will serve as reference for all the simulations and experiments presented in this work. For this, we first recall the characteristics of a downlink propagation. Then, we explain how an AO system compensates the downlink phase aberrations induced by turbulence and how we use this information to pre-compensate the uplink, and the limitations of this pre-compensation. We then describe the uplink propagation. Finally, we describe the simulation model used to obtain ROP time series and we present the scenarios that are used for the rest of the study.

A. Downlink Beam Propagation

In a typical optical link connecting a geostationary (GEO) satellite to the ground downwards, the field profile from a single mode fiber is expanded, truncated by the satellite telescope pupil, and propagates in vacuum until it reaches the upper atmosphere. Because of the very long propagation distances, the field entering the atmosphere can be locally approximated by a plane wave. Then, it propagates through layers of air with spatially varying index of refraction. The layers move with respect to each other and produce the so called "optical turbulence", which translates into fluctuations of the wavefront and of the field amplitude. As a result, at the ground station pupil, a distorted optical field is received. The strength of the turbulence is locally characterized by the refractive-index structure constant (C_n^2) and the overall strength along the line of sight is given by the Fried parameter (r_0) [20], which also quantifies the coherence length of the disturbed complex field.

B. Adaptive Optics System

An adaptive optics system compensates for the phase of the aberrated field in the pupil plane to maximize the coupled power. The AO is composed of three main components: a deformable mirror, a wavefront sensor and real-time controller [21], [22], as shown in Fig. 1. First, the aberrated field is reflected by the deformable mirror, then it is separated in two paths using a beam

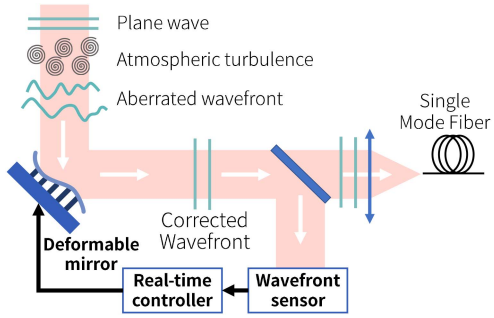

Fig. 1. Adaptive Optics (AO) system loop for phase aberrations compensation.

splitter. One beam is coupled into a single-mode fiber and the other is sent to the Shack-Hartmann wavefront sensor. Finally, the wavefront sensor measurements are used by the real-time controller to drive the deformable mirror in a feedback loop. The Shack Hartmann sensor senses the incoming wavefront using a finite number of sub-apertures, we assume then that the deformable mirror corrects a limited number of Zernike modes [23]. In our simulations, we consider a two-sampling time delay AO loop and an integral controller (setting the gain to 0.5).

Compensation by AO strongly reduces fluctuations of the power coupled in the single mode fiber but does not fully cancel them, owing to two mains causes. The first cause is amplitude fluctuations in the pupil, which are not corrected by classical AO, also called scintillation. The second is imperfect phase correction by AO due to residual temporal, fitting and aliasing errors [24]. Temporal error is induced by the delay between the sensor measurements and the actual compensation execution and is therefore related to the dynamics of the atmosphere and the frequency of the AO loop. Fitting errors originate from the limited number of modes that the AO can correct. Aliasing is consequence of the limited size and number of sub-apertures of the wavefront sensor.

C. Uplink Beam Propagation

The beam of a typical GEO uplink direction propagates first in the atmosphere and then in vacuum up to the satellite. In the satellite plane, the coherence length of the field is of the order of hundreds of meters, however, the irradiance pattern fluctuates in shape (beam spread) and in position (beam wander) [25], [26]. The spatial distortions expand as the wavefront propagates upwards and become much greater than the pupil (telescope) size. As a result, the pupil receives a quasi-planar wavefront, so that an AO system is ineffective at satellite receiver side.

Despite the different propagation geometries, the reciprocity principle states that two beams propagating in opposite directions along the same line of sight produce the same coupled power series, only delayed by the propagation time [27], [28]. This fundamental principle suggests that AO could pre-compensate for the distortions of an uplink beam by reading the wavefront distortions of the downlink beam acquired over the same path.

However, due to the relative motion speeds between the satellite and the ground station, the uplink beam must be deviated by a point ahead angle (few 10 μrad) from the downlink. Hence the downlink and the uplink do not share the exact same path. Consequently, they suffer from the anisoplanatism effect, whereby they experience two distinct turbulence conditions [29]. This effect degrades the performance of the AO pre-compensation [19], [30], [31]. Despite anisoplanatism, adaptive optics helps to increase the mean received power and to decrease the irradiance variance of the uplink but leaves potentially strong attenuation peaks uncorrected [32], [33].

Anisoplanatism is characterized by the anisoplanatic angle θ_0, which quantifies the turbulence angular correlation. It is primarily determined by the higher atmospheric layers, where the distance between the paths is greater. A smaller θ_0 corresponds to a weaker correlation between the pre-compensation and the state of the turbulence, and then leads to deeper residual attenuation peaks at the receiver. Due to the finite receiver sensitivity and the limitations of the transmitter optical amplifier power (a few tens of Watts for single amplifiers [34] and a few hundreds of Watts for coherent combinations [35]), the power drops create error bursts when the ROP falls below the reception threshold, also known as fading. At the same time, the duration of these attenuation peaks is defined by the high-altitude wind speed. The impact of this aspect is studied in Section V.

D. Simulation Scenarios

Atmospheric turbulence effects are then modelled by discretizing the atmosphere in multiple phase-screens and propagating the beam through them with a split-step computation method [36], [37]. Here, we use an experimentally validated simulation tool [38] to generate ROP time-series at the reception terminal. We import the C_n^2 profile, which sets the strength of the turbulence at each altitude, and consequently in each phase screen. We then represent the dynamic nature of the turbulence by translating each phase-screen horizontally, assuming that the screen pattern remains unchanged (this is the frozen flow hypothesis). Overall, the distortions to the beam depend primarily on the selection of the most relevant C_n^2 and wind profiles.

The strength of the turbulence is stronger at low altitudes and in daytime conditions because of interactions between the atmosphere and the ground. However, most of the available data bases aggregating field measurements at astronomical sites were recorded in nighttime conditions. Aiming at considering the more demanding daytime scenarios, we use turbulence profiles generated from two different data bases as described in [39]. The C_n^2 values for the upper layers are obtained from day and night measurements at Cerro Paranal at different altitudes [40], assuming that the turbulence strength of the higher layers is independent of the diurnal cycle. The lower turbulence profile is generated using daytime measurements at 30 m above ground in the Canary Islands [41], and a Monin-Obhukov similitude law [42]. With these measurements, we generate multiple C_n^2 profiles representing different turbulence strength conditions. In this work we select the stronger scenario shown in Fig. 2 of [39], which corresponds to a Fried parameter of 4 cm and an anisoplanatic angle equal to 6.8 μrad along the line of sight at 30 degrees of elevation and at 1550 nm. We use this profile to compute the time series used in the rest of the paper.

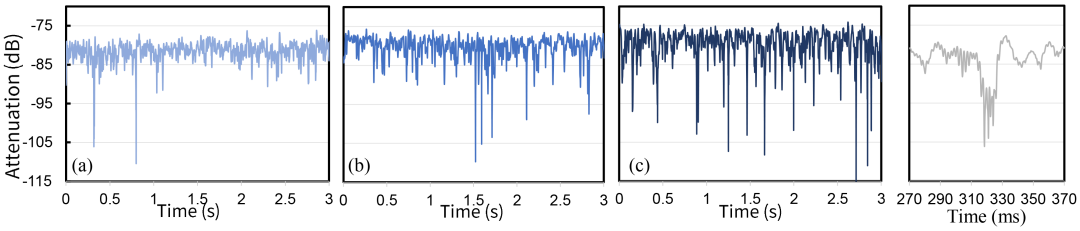

Fig. 2. Received optical power (ROP) time-series for pupils of (a) 30, (b) 40 and (c) 60 cm, for scenario 3), and 0 dBm of launch power. (d) An inset of the first fading extracted from the time-series (a).

TABLE I
SIMULATED SCENARIOS

Scenario	$V_g\ (m/s)$	$V_t\ (m/s)$
1	10	15
2	10	30
3	14	20

Here, our baseline scenario is an optical transmission from a ground station to a geostationary (GEO) satellite at 30 degrees elevation and using pre-compensation by AO with a point-ahead angle of 18.5 μrad. For the wind profile, we use a Bufton model which is characterized by the wind speed at low altitude (V_g), the wind speed at the tropopause (V_t), the altitude of the tropopause (h_t) and the thickness of the tropopause (L_t) [43], [44]. We estimate the static losses induced by Tx and Rx optics losses, clouds, and aerosols attenuation, and pointing error at 16 dB as presented in [39]. We compute the field received by the satellite telescope, with a split-step method while accounting for the above strong turbulence scenario and, with AO pre-compensation in the presence of point-ahead anisoplanatism. From this field we can obtain the power coupled into the single-mode fiber by calculating the square modulus of the overlap integral between this field and the fiber mode [45], [46]. As the coherence length of the beam is longer than the pupil diameter, we can consider the amplitude and wavefront as constant. To maximize the coupling efficiency, we set $\mathrm{D_{RX}}/\omega_0^{\mathrm{P}} = 2.2$ [47], with ω_0^P the value of the mode waist brought to the pupil plane and D_{RX} the reception pupil diameter. In the same way, we set the ratio D_{TX}/ω_0^P at the ground station equal to 2.2. Here, we set the diameter of the satellite reception pupil to 25 cm.

We first investigate the impact of the ground and troposphere wind speed on the fading distribution and duration. For this, we set the value of h_t to 12 km and the L_t to 4.8 km, we then select three different scenarios varying the value of v_g and v_t based on wind measures presented in [48]. Table I summarizes the three studied cases. Scenarios 1) and 2) were selected to illustrate the intuition that temporal behavior of the ROP time series and fadings duration are primarily determined by high-altitude winds. The third scenario involves a high-speed low-altitude wind, hence with a stronger impact of temporal effects on the AO pre-compensation. In all cases, the speed of the AO loop is set to 4.7 kHz. It should be noted that in the Bufton profile the wind speed at the troposphere altitude corresponds to the sum of v_g and v_t, then, scenario 3) also represents an intermediate high-altitude wind speed between the scenarios 1) and 2).

To consider the impact of different pupil sizes, we simulate different ground station pupil diameters: 30 cm, 40 cm, and 60 cm. The corresponding number of sub-apertures across the diameter, and the maximum Zernike radial order of the adaptive optics for the correction are 10, 14, 20 and 8, 12, 18 respectively. We adjust the number of corrected radial orders to obtain a fitting error about 0.14 rad^2, adapting the number of sub-apertures to fulfill this condition.

Fig. 2(a)–(c). shows a snippet of 3 seconds of the simulated ROP timeseries at the satellite in scenario 3), considering the geometrical losses and the static channel losses, for the three pupil diameters, for a launch power of 0 dBm. We also show in Fig. 2(d) an inset of a fading to illustrate the typical duration of such an event. The geometrical loss induced by the divergence of the emitted beam is different for each pupil diameter, at 55.7 dB, 59.0 dB and 61.5 dB, for the pupil of 60 cm, 40 cm, and 30 cm respectively. Despite lower geometrical loss for larger telescopes, we can see that, owing to beam wandering, the 60 cm pupil generates deeper attenuation peaks. Hence, the optimal telescope diameter depends on whether the receiver is more affected by a lower mean ROP or by deeper fading peaks, as investigated below.

III. DIMENSIONING BLOCK INTERLEAVERS

The atmospheric turbulence induces power drops with up to a few ms duration which can eventually create error bursts. Standard FEC cannot correct these error bursts which could last several thousands of FEC codewords. One of the ways to overcome this problem is to use interleaving, which distributes the errors over a longer duration, called interleaver time.

The most frequently used interleaver types for the communication standards DVB [49], [50], [51] and ATSC [52] are block interleaver type and convolutional interleaver type. A convolutional interleaver with similar dimensions of a block interleaver would bring very similar performance, with the important advantage of inducing only half the delay [53]. Both interleavers types require a high-capacity and high-speed memory, like synchronous dynamic random-access memory (SDRAM) [54], [55]. For our proof-of-concept, we use a DDR3 SDRAM memory, which is a mature technology and meets the transfer rate requirements for 10 Gbps transmissions. However, interleaving requires simultaneous read/write processes which decrease considerably (e.g., by more than half) the transfer rate of this type of memory [56]. Therefore, we chose the block interleaver type over the convolutional interleaver type, at the expense of latency, because it allows for easier dual buffering, hence avoids writing

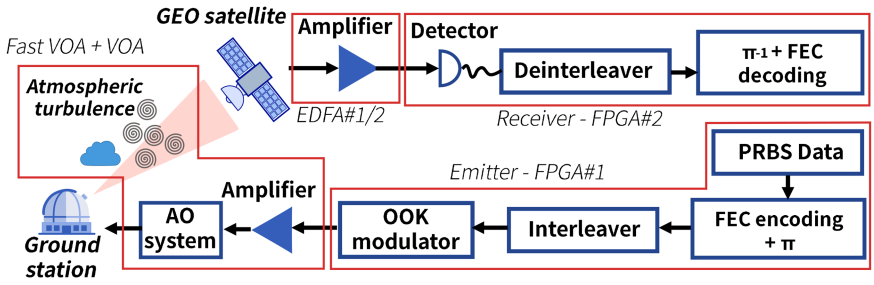

Fig. 3. The optical communication chain for ground-to-satellite transmissions with FEC, π interleaving, ms interleaving and AO precompenation. The components used in the experimental setup to emulate each stage of the communication are framed in red squares.

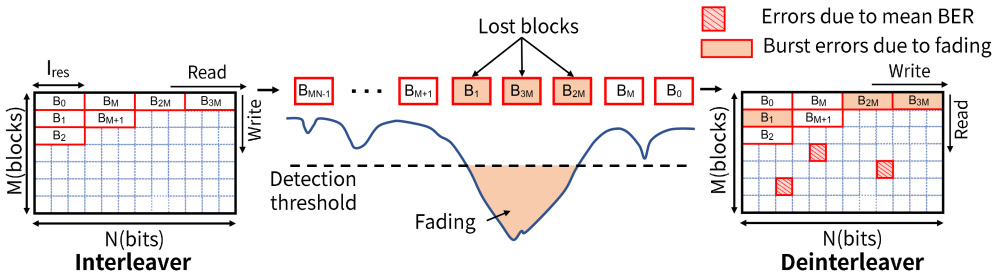

Fig. 4. (a) MxN block interleaver (left) and deinterleaver (right) with blocks of size I_{res}. At the interleaver stage, new data blocks are written into columns and read from lines. ¸At the deinterleaver stage, data blocks are written into lines and read from columns.

and reading from/into the same memory region in short time periods (e.g., 5–50 ns). For latency reduction with convolutional interleavers or operation at higher data rate, new memory technologies should be contemplated, such as High Bandwidth Memories SDRAM [57].

In the following, we propose a method to dimension our block interleaver based on the ROP time series. Then we discuss whether the classical indicators like the average fading time and the average inter-fading time are insightful criterions for the design of interleavers. In Fig. 3, we depict an uplink communication system traversing the atmosphere along with data encoding and decoding blocks.

We consider a block interleaver with M rows and N columns, and we interleave by blocks of bits of size I_{res}, which we call resolution hereafter. For a bit rate of R_b, the interleaver time is given by $(M \times N)/R_b$. In the left part of Fig. 4. we show an MxN interleaver write-read process. In the central part, we schematize a few consecutive blocks affected with an error burst from a power fading. In the right part, we show how these erroneous blocks are redistributed in the deinterleaver matrix. We assume random distributed errors caused by the noise at the sides of the fading.

Without loss of generality, we assume that any interleaver matrix contains e_b burst errors generated by a continuous fading, while the other bits have a mean bit error rate (BER) of $\overline{BER}$ as shown in Fig. 4. To distribute the errors uniformly over all the FEC codewords in the interleaver matrix, we set the value of M as follows:

$$M = \left\lceil \frac{FEC_N}{I_{res}} \right\rceil \text{(bits)} \tag{1}$$

where FEC_N is the size of the FEC codeword and $\lceil . \rceil$ denotes the ceiling function. Assuming a continuous e_b, the maximum number of burst errors per FEC codeword e_{FEC_b} is given by

$$e_{FEC_b} = I_{res} \times \left\lceil \frac{e_b}{N} \right\rceil \tag{2}$$

Assuming a constant mean bit error rate $\overline{BER}$ for bits outside burst periods, the total number of errors per FEC codeword can be estimated using

$$e_{FEC} = e_{FEC_b} + \overline{BER} \times (FEC_N - 2e_{FEC_b}) \tag{3}$$

Given that a FEC can correct up to $BER_{FEC} \times FEC_N$ errors, with BER_{FEC} the pre-FEC BER threshold, the number of errors per codeword must fulfill the following condition:

$$e_{FEC} \leq BER_{FEC} \times FEC_N \tag{4}$$

Thus, substituting (2) and (4) in (3), we can calculate the value of N to guarantee the decoding condition of the FEC:

$$N \geq \left\lceil I_{res} \times \frac{e_b\left(1 - 2\overline{BER}\right)}{FEC_N\left(BER_{FEC} - \overline{BER}\right)} \right\rceil \tag{5}$$

which is valid when $\overline{BER}$ is lower than BER_{FEC} threshold.

For better insight into the interleaver design, we define the interleaver resolution-codeword size ratio (IRCSR) as:

$$IRCSR = \frac{I_{res}}{FEC_N} \tag{6}$$

If a fading is longer that the interleaver resolution, independently of the value of N, e_{FEC} will be higher than $0.5 \cdot I_{res} + \overline{BER}(FEC_N - I_{res})$. After replacing this expression in (4) we

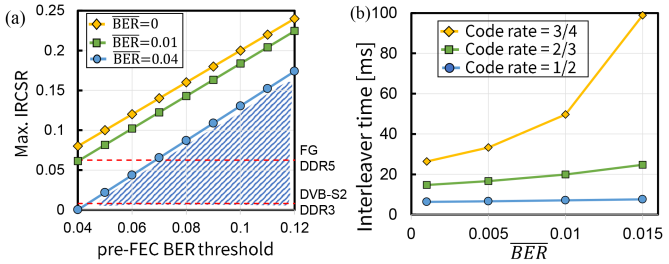

Fig. 5. (a) Maximal interleaver resolution-codeword size ratio (IRCSR) for different mean BER. Red dotted lines indicate IRCSR for two typical FECs and memory types. (b) Interleaver time for different FEC code rates for fading of 1 ms.

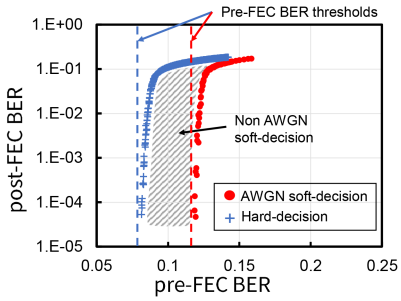

Fig. 6. Post-FEC BER as a function of the pre-FEC BER for hard decision de-mapping and soft-decision de-mapping for an AWGN channel, considering the DVB-S2 FEC with ADC resolution of 6 bits, code rate of 1/2 and maximum iterations of 25.

find the following upper bound for IRCSR:

$$\text{IRCSR} \leq \frac{BER_{\text{FEC}} - \overline{\text{BER}}}{0.5 - \overline{\text{BER}}} \ \text{(bits)} \tag{7}$$

The interleaver adds some latency which depends on the size of the matrix. The input blocks are written along the columns, then, the blocks can be read from the rows when the first block of the last column has been written. At the reception, the received blocks follow the same process. Thus, the delay induced by the interleaving/deinterleaving process is given by the following equation:

$$\text{delay} = \frac{2}{\text{R}_\text{b}} \left(\text{N} \times \text{M} - \text{I}_\text{res} \left(\text{M} + 1\right)\right) \ \text{(s)} \tag{8}$$

The minimum interleaver time t_inter required to achieve an error-free transmission can be calculated by converting (5) to an equality, multiplying it by (3) and dividing the result by the bit rate:

$$\text{t}_\text{inter} = \frac{1}{R_b} \left\lceil \frac{\text{e}_\text{b} \left(1 - 2\overline{\text{BER}}\right)}{\left(\text{BER}_\text{FEC} - \overline{\text{BER}}\right)} \right\rceil (s) \tag{9}$$

As we can see, this value depends only on three parameters: the length of the burst error generated by the fading, the average BER outside the fading and the pre-FEC BER threshold. Although the size of the interleaver does not depend on the resolution I_res or the size of the codeword FEC_N these parameters define the shape of the interleaver matrix and restrict the range of validity of (9), as shown in (7).

Fig. 5(a) represents the boundary conditions for the interleaver design. In full line, we report the maximum admissible value of the IRCSR as a function of the hard decision pre-FEC BER threshold, calculated using (7), for three values of $\overline{\text{BER}}$. This limit should not be taken as an absolute value, but rather as a threshold from which the designer should stay away from. The closer the system is to this limit, the more vulnerable it is to the increase of $\overline{\text{BER}}$. For instance, in a system impaired by noise producing $\overline{\text{BER}} = 0.04$ any combination of interleaver resolution I_res and codeword length FEC_N in the shaded region of Fig. 5(a) can produce error-free performance. However, this combination should account for the SDRAM characteristics. In particular, SDRAM memories use large bus interfaces and consecutive transmissions (prefetch). DDR3 and DDR4 SDRAM have a minimum bus width of 64 bits and prefetch of 8 [58], [59], yielding a minimum interleaver resolution of 512 bits. DDR5 SDRAM has the same minimum bus width, but a prefetch of 16 [60], which sets the minimum interleaver resolution to 1024 bits. In the example of a configuration based on DDR3 memory and DVB-S2 FEC encoding [50] with codeword lengths of 64800, IRCSR amounts to 0.008 and Fig. 5(a) shows that the pre-FEC BER threshold has a bottom limit at 0.04, for $\overline{\text{BER}} = 0.04$. By contrast, in the example of a configuration based on DDR5 and Finite Geometry (FG) FEC encoding [13] with codeword length of 16384, IRCSR would amount to 0.062 and the pre-FEC BER threshold has a higher bottom limit at 0.07.

We now compute the interleaver time as function of the pre-FEC BER threshold and the $\overline{\text{BER}}$ using (9). We consider the DVB-S2 standard FEC as reference ($\text{FEC}_\text{N} = 64800$), with hard decision decoding yielding pre-FEC BER thresholds of 0.08, 0.035, 0.02 for code rates 1/2, 2/3 and 3/4, respectively, at a post-FEC BER of 10^{-9}. In Fig. 5(b), we report the interleaver time assuming a 1 ms fading time and for resolution $\text{I}_\text{res} = 512$ bits. We can see that FEC with lower correction capacity, e.g., when high code rates are selected, require longer interleaver times and are more impacted by the variation of the mean BER.

One important subject of concern is the assessment of the pre-FEC BER threshold BER_FEC. If the signal was subject only to additive white Gaussian noise (AWGN), it could be easily derived from textbooks through the post-FEC BER versus pre-FEC BER curves [61], [62]. We computed and reported in Fig. 6 such curve for the DVB-S2 standard FEC [50], with soft decision de-mapping assuming an ADC resolution of 6 bits, a code rate of 1/2, and a maximum of 25 iterations. In the atmosphere channel affected by turbulence, Fig. 4 recalls that, each codeword at the receiver is impaired not only by errors from AWGN (primarily from optical amplifiers) but also errors from fadings. We may still assume that the errors are randomly distributed, because we implement a second interleaving (π interleaver) within each codeword, but the probability density function of the received samples departs from Gaussian. Consequently, the error correction capabilities of FECs, optimized for AWGN conditions, are degraded. The resulting penalty cannot be assessed for all turbulence conditions because it depends on the occurrence, width, and depth of fadings. In the absence of such an a priori knowledge, we reworked the reference curve to make it an upper bound for all turbulence

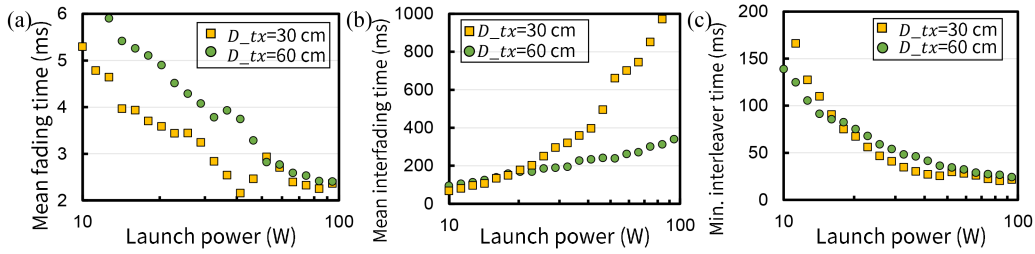

Fig. 7. For pupil diameter of 30 and 60 cm, and scenario 3. (a) Mean fading time vs launch power. (b) Mean interfading time vs launch power. (c) Mean minimum interleaver time vs launch power.

conditions. To this end, we perform hard decision de-mapping but still undergo the error correction algorithms of the DVB-S2. We added in Fig. 6 the post-FEC BER calculated in these conditions as a function of the pre-FEC BER. We can see that the pre-FEC BER limit for the AWGN channel is ∼0.12, while for the hard decision de-mapping case the value is ∼0.08. To stay on the safe side of the interleaver design and taking into account the limitations of our implementation, which does not incorporate any analog to digital converter, we perform hard decision de-mapping in the simulations as well as in the experiments of this paper.

Known metrics used to study power time series are fading and interfading time [16], [17], [18]. Based on these metrics a favorable time series is the one with low mean fading time and a high mean interfading time. However, these metrics do not consider the value of the mean BER and could lead to underestimations, especially for high code rates and when the $\overline{\text{BER}}$ is large, as we can see in Fig. 5(b)

Fig. 7. shows the mean fading time (a), mean interfading time (b) and mean minimum interleaver time (c) for two time series with 30 cm and 60 cm pupil diameter of the scenario 3, and for a detection threshold of -45 dBm, as a function of the launch power. To calculate the mean of the minimum required interleaver time, we use our method for calculating the fading time and mean BER for each fading in the series, then, we computed the mean of these values and finally, we find the minimum required interleaver time. Fig. 7(a) and (b) show that the 30 cm pupil has lower mean fading time and similar mean interfading time for launch powers below 20 W, suggesting a better performance of this pupil. However, in this region, since the geometric losses are higher for the smaller pupils, the mean power is closer to the detection threshold, and so, the mean BER is more significant. In Fig. 7(c) we can see that the mean minimum interleaver time is lower for launch powers higher than 20 W for the 30 cm pupil. However, for low launch powers (less than 20 W), where the average noise is more important, the smaller telescope becomes undesirable.

IV. Experimental Demonstration

To verify the proposed interleaver dimensioning method, we set-up the real-time demonstrator presented in Fig. 8. We implement a real-time block interleaver and deinterleaver on two VC709 FPGA boards each equipped with 2 DDR3 SDRAM memories with a capacity of 32 Gbits and a maximum data

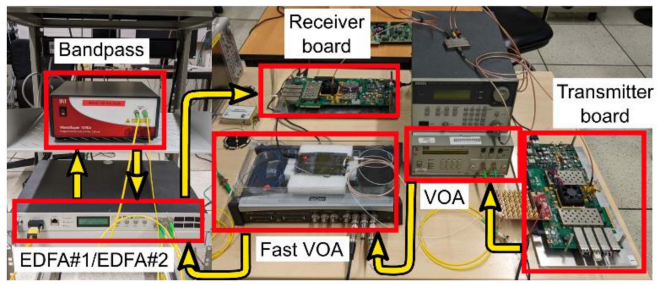

Fig. 8. Experimental apparatus emulating a free space optical link communication system.

transfer rate of ∼100 Gbps. At the transmitter side, we generate in Matlab a FEC codeword using the DVB-S2 encoding and a 16-PRBS data stream. Then, we use a block interleaver (π) as the one used in the DVB-S2 standard but with the number of columns adapted to burst errors of the interleaver resolution size ($\sim M \geq I_{res}$) to guarantee uniformly distributed errors within each codeword. The resulting codeword is stored in the transmitter board, and continuously read and interleaved with a resolution of $I_{res} = 512$ bits. To help with the interleaver-deinterleaver synchronization, we implemented a specific framing function which adds headers (1% overhead) containing the block order information. The resulting data stream is modulated with on off keying by an SFP+ optical transceiver module and transmitted with an optical power of ∼1 dBm. While the data rate is relatively moderate at 10 Gbps, the transmitter/receiver architecture was defined so as to comply with the requirements of +100 G systems where the interleaver memory exceeds the capability of foreseen coherent ASICs and therefore needs to be part of a separate chip.

The optical signal is sent to a variable optical attenuator (VOA) which emulates the static channel losses by attenuating between 37 dB, for a launch power of 10 W and a 30 cm pupil (61.5 dB of geometric losses), and 11 dB, for 1000 W of launch power and a 60 cm pupil (55.7 dB of geometric losses) depending on the transmission pupil size and the launch power. Then, a fast VOA (5 kHz bandwidth) is fed by the time-series described in Section II-D to emulate the dynamic effects of the atmospheric turbulence by generating attenuation peaks with values up to 25 dB as shown in the Fig. 2.

At the reception, the signal is pre-amplified using an Erbium Doped Fiber Amplifier (EDFA) #1, filtered (50 GHz) to perform amplifier noise rejection and amplified by EDFA#2 as show

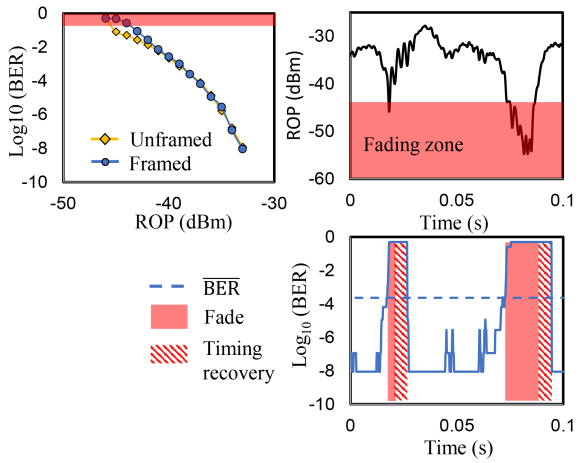

Fig. 9. (a) The dependence of the measured BER with ROP, with and without interleaver framing. (b) A snippet of a time series of 100 ms with the fading zone in red. (c) BER of the time series.

in [63]. The input power range of the first EDFA is between −15 dBm and −60 dBm, depending on the considered launch power and the selected pupil diameter. The noise figure of both EDFAs is measured to be about 4.5 dB. While the EDFA#1 is configurated to work with a constant current and its output power varies between −20 dBm and 5 dBm, the EDFA#2 works in saturation mode and provides a constant power of ∼8 dBm. Finally, a constant attenuator adjusts the power to 1 dBm before the SFP+ module at the reception board.

The receiver board uses the interleaver frame header information to align the incoming bit stream, then, it is deinterleaved and sent to Matlab for post-processing. We store up to 1 s of deinterleaved data into the DDR3 memories in the reception board (∼10 Gbps), we then use an UART interface to send this data to Matlab, where each codeword is deinterleaved (π^{-1}), the pre-FEC BER is calculated, and the data is decoded to obtain the post-FEC BER.

The interleaver frame is composed of groups of 6144 bits and a 64 bits header. The header has an identifier of 30 bits equal to "318D2E82" (corresponding to the physical layer frame signaling of the DVB-S2) and 31 bits containing the frame position information. This information corresponds to a 25 bits counter encoded by a Hamming code, to correct up to 1 error and detect up to 2 errors. At the reception a header is identified if 28 bits or more of the 30 bits corresponds to those of the identifier. Therefore, if the BER is too high, some headers could be ignored, causing frame desynchronization. This problem can arise also if after header identification, erroneous address is read. Hamming encoding helps to reduce this source of errors.

In the static regime, the BER of the received data was measured as a function of the ROP with and without the interleaver framing, as shown in Fig. 9(a). We can see that the alignment method causes the BER to saturate rapidly after −44 dBm. We found that when the ROP falls below a threshold of −45 dBm the receiver loses the clock reference and typically recovers around $0.7 \pm 0.3\ ms$ after it rises above this threshold.

To calculate the interleaver time, we first estimate the fading time and the ($\overline{\text{BER}}$) from the generated time series. To do this, we look for fadings in a 100 ms window as shown in Fig. 9(b). Then, using the measured ROP to BER curve with interleaver framing (Fig. 9(a) circles blue line) we calculate the BER in the window and add the time recovery as shown in Fig. 9(c). The fading time corresponds to the segments which are shown in red (solid and line pattern) and the mean BER (dashed line) was calculated in the segments with BER less than 0.5. We found that ($\overline{\text{BER}}$) typically lies between 0.001 and 0.01. By increasing the launch power, the fading time decreases but even for a launch power of 60 W, we observed that fading times vary between 1 and 15 ms.

We now measure experimentally the required interleaver time by varying the interleaver time until all the codewords after the interleaver have a BER below the pre-FEC limit. In the upper part of Fig. 10(a), we show a snippet of the ROP series for a pupil diameter of 30 cm and for scenario 1, together with the reception threshold (−45 dBm) and the pre-FEC BER limit (0.08). The lower part shows the measured pre-FEC BER after the deinterleaver for an interleaver time of 81 ms. We can see how each interleaver window averages the errors along its duration. The calculated interleaver time for this time series is 102 ms, given that the implemented interleaver time is much lower, we obtained a non-zero post-FEC BER in the highlighted region. By increasing the interleaver time to 95 ms, all the codewords satisfy the FEC condition and the post-FEC BER is lower than 10^{-9} for all the codewords.

This whole process is repeated for each fading event for different time series, varying its position in the interleaver window and using the pre-FEC BER as metric. In Fig. 10(b), we show the measured required interleaver times (crosses) for various fading times along with the calculated ones (blue circles), using (8). The measurements fall within +/−10% of the calculations in up to 83% cases. The residual error could be attributed to the presence of multiple fadings or to the position of the fading into the calculation window, given that for the calculations we assume a continuous fading event in the middle of the window. Also, the $\overline{\text{BER}}$ was underestimated because of the averaging of a long initial window. By iteratively modifying the size of the windows, we increase the cases into the +/−10% interval to 95%.

We estimated the minimum interleaver time for different pupil sizes and then obtained best performance for a pupil size of 40 cm which will be elaborated in the next section. For various launch powers, we calculate the minimum interleaver time for the worst fading event over all the time series for D = 40 cm and wind scenario 1, and the results for different code rates are shown in Fig. 10(c). We can see that even for large launch powers an interleaver is necessary for error-free transmissions under strong turbulence. We observe that an interleaver of 150 ms can bring a reduction of two orders of magnitude, making it feasible to use a commercially available amplifier of 30 W [64] to establish a net rate of 5 Gbps links using a code rate of 1/2. If we increase the code rate, much higher launch power (>100/300 W) is required to allow a transmission using the same interleaver time.

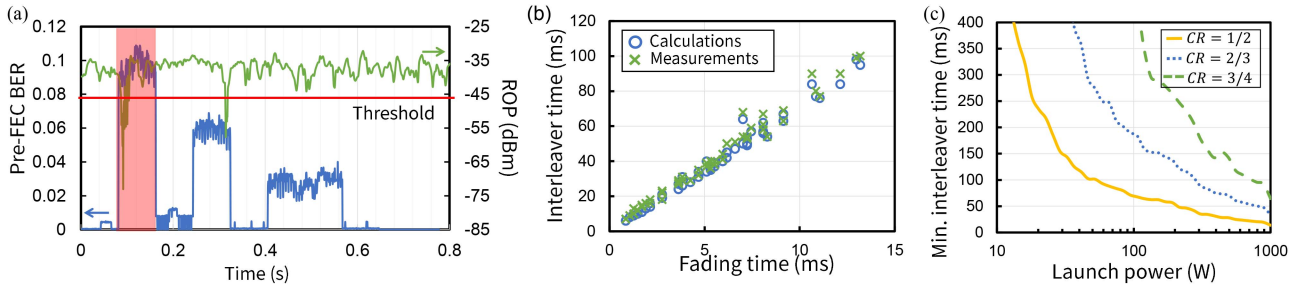

Fig. 10. (a) Received optical power time-series (up) and obtained pre-FEC BER (down), with the reception threshold and DVB-S2 FEC 1/2 pre-FEC BER limit (red line for both). (b) The calculated (blue circles) and measured (green crosses) interleaver time for different fadings from the time series. (c) The minimum calculated interleaver time as a fuction of the launch power for different DVB-S2 code rates for a pupil size of 40 cm and the scenario 1.

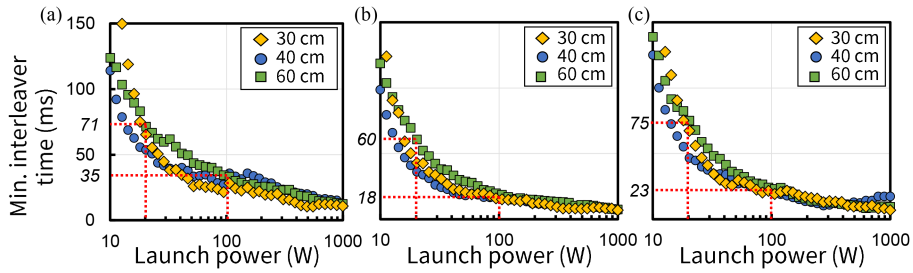

Fig. 11. The mean minimum interleaver time for the three different pupils and for wind scenarios 1(a), 2(b) and 3(c).

V. Impact of Pupil Diameter and Wind Speed

In this section, we study the impact of the wind speed on the interleaver duration for different transmission pupil diameters. For this, we use the different wind speed scenarios presented in Table I and we vary the launch power, then, we use our dimensioning method and the time series described in the Section II-D (accounting for AO pre-compensation) to find the mean minimum required interleaver time.

While high speed wind for low altitude produces fast variations of the downlink received field and demands a rapid AO loop to follow these variations, the uplink beam pre-compensation is mainly degraded by the higher atmospheric layers because the anisoplanatism. As the dynamic of the turbulence is driven by the wind speed, we can expect longer fadings for lower high-altitude wind speeds, then longer interleavers.

Fig. 11(a) and (b), and (c) shows the mean minimum required interleaver time as a function of the launch power for the three pupil diameters and for the three wind speed scenarios: 1, 2 and 3 respectively. We also plot the longest interleaver time for 20 W and 100 W of launch power to facilitate comparison. In Fig. 11(a) and (b), we can observe the impact of high-altitude wind speeds by comparing the scenarios 1 ($V_t = 15$ m/s) and 2 ($V_t = 30$ m/s) (with the same $V_g = 10$ m/s). We can see that lower high-altitude wind speed yields a longer interleaver time for different pupil diameters and launch powers.

We can also see that, for launch powers higher than 20 W, the 60 cm pupil usually requires longer interleaver time due to the presence of adjacent fadings. When the launch power increases, the difference curves tend to converge as the impact of the mean noise becomes negligible and the fadings are more spaced for all pupils, then, the interleaver calculation corresponds with that of a single fading with $\overline{\text{BER}} \approx 0$. On the other hand, for low launch powers where the fading side noise becomes important, the 30 cm pupil is highly undesirable due to its large geometrical losses.

VI. Conclusion

In this article we presented a proof of concept of an optical satellite uplink involving adaptive optics pre-compensation, and strong FEC and an interleaver implemented in an DDR3 external memory. We generated representative ROP time series for a ground-to-GEO satellite link using an experimentally validated simulator fed with representative daytime turbulence profiles. Then, we calculate the interleaver time which guarantees error free transmissions for different fadings distributions. We implemented a real-time communication testbench where the high-speed interleaver memory is located next to the communication module, but in a different chip, as foreseen in future high-throughput optical satellite systems across atmosphere. With 10 Gbps OOK, we found that our calculations fall within $+/-10\%$ of the calculations in up to 95% cases. We then compared the obtained interleaver time with the fading and interfading time metrics. We found that these metrics could underestimate the impact of optical amplifier, especially when the reception threshold is close to the mean reception power.

We used our method to calculate the required interleaver time as a function of the launch power, assuming DVB-S2 FEC and different code rates, and we found that even if we increase the launch power up to 1000 W, an interleaver of some ms is necessary. Also, we showed that a 30 W amplifier allows to establish an error-free transmission using a 150 ms interleaver and a 1/2 code

rate. Finally, we studied the impact of high-altitude wind speed on the interleaver duration. We showed that slow wind speed in higher layers generates longer fadings and represents the most challenging scenario. Finally, when comparing pupil sizes of 30, 40 and 60 cm, we found that 30 cm pupil is undesirable for low launch powers (< 20 W) and 60 cm pupil has the worst overall performance.

Acknowledgment

We thank James Osborn (Centre for Advanced Instrumentation, Durham University) for kindly providing the turbulence profile data base described in [40].

We thank Nicolas Védrenne and Vincent Michau for their support and fruitful scientific discussions.

References

[1] G. Artaud, B. Benammar, D. Juglet, L. Canuet, and J. Lacan, "Impact of molecular absorption on the design of free space optical communications," *Proc. SPIE*, vol. 11180, pp. 544–554, 2018.

[2] S. Almonacil, R. Boddeda, and S. Bigo, "Experimental study of the impact of molecular absorption on coherent free space optical links," in *Proc. Eur. Conf. Opt. Commun.*, 2020, pp. 1–4.

[3] D. R. Arrieta, R. Boddeda, S. Almonacil, T. Allain, and S. Bigo, "Capacity limits of optical satellite communications," in *Proc. Eur. Conf. Opt. Commun.*, 2020, pp. 1–4.

[4] S. Trisno, I. I. Smolyaninov, S. D. Milner, and C. C. Davis, "Characterization of time delayed diversity to mitigate fading in atmospheric turbulence channels," *Proc. SPIE*, vol. 5892, 2005, Art. no. 589215.

[5] H. Méric and L. Péricart, "Performance evaluation of a DVB-S2 system with a digital optical feeder link," *Int. J. Satell. Commun. Netw.,* vol. 38, no. 6, pp. 463–479, 2020.

[6] Y. Q. Shi, X. M. Zhang, Z.-C. Ni, and N. Ansari, "Interleaving for combating bursts of errors," *IEEE Circuits Syst. Mag.*, vol. 4, no. 1, pp. 29–42, 2004.

[7] P. Klenner, J.-S. Baek, N. S. Loghin, D. Gómez-Barquero, and W.-S. Ko, "Physical layer time interleaving for the ATSC 3.0 system," *IEEE Trans. Broadcast.*, vol. 62, no. 1, pp. 253–262, Mar. 2016.

[8] A. Carrasco-Casado and R. Mata-Calvo, "Space optical links for communication networks," in *Springer Handbook of Optical Networks*, B. Mukherjee, I. Tomkos, M. Tornatore, P. Winzer, and Y. Zhao, Eds. Cham, Switzerland: Springer, 2020, pp. 1057–1103.

[9] D. R. Arrieta et al., "Block interleaver dimensioning and real-time demonstration for ground-to-satellite optical communications," in *Proc. Eur. Conf. Opt. Commun.*, Basel, Switzerland, 2022, pp. 1–4.

[10] N. Mazzali and P.-D. Arapoglou, "Channel interleaver dimensioning for optical LEO direct-to-earth systems," in *Proc. 10th Adv. Satell. Multimedia Syst. Conf. 16th Signal Process. Space Commun. Workshop*, Graz, Austria, 2020, pp. 1–6.

[11] S. Poulenard et al., "Forward error correcting code for high data rate LEO satellite optical downlinks," *Proc. SPIE*, vol. 11180, 2019, Art. no. 111805L.

[12] M. Chochol, A. Rissons, J. Lacan, N. Vedrenne, and G. Artaud, "Evaluation of error correcting code performances of a free space optical communication system between LEO satellite and ground station," *Proc. SPIE*, vol. 9647, 2015, Art. no. 96470K.

[13] S. Poulenard, B. Gadat, L. Barthe, and R. Garzón-Bohórquez, "Protection schemes for optical communication between optical ground station and a satellite," in *Proc. Workshop (Commun. Observ. Through Atmospheric Turbulence: Characterization Mitigation)*, Châtillon, France, 2019, pp. 1–8.

[14] J. Osborn, M. J. Townson, O. J. D. Farley, A. Reeves, and R. Mata Calvo, "Adaptive optics pre-compensated laser uplink to LEO and GEO," *Opt. Exp.,* vol. 29, no. 4, pp. 6113–6132, 2021.

[15] L. B. Stotts and L. C. Andrews, "Bit error rate performance of a laser ground-to-satellite uplink communications systems in the presence of atmospheric turbulence and loss," in *Proc. IEEE Int. Conf. Space Opt. Syst. Appl.*, Kyoto City, Japan, 2022, pp. 66–73.

[16] L. Canuet, N. Védrenne, J.-M. Conan, G. Artaud, A. Rissons, and J. Lacan, "Evaluation of communication performance for adaptive optics corrected geo-to-ground laser links," *Proc. SPIE*, vol. 10562, 2017, Art. no. 1056248.

[17] L. Canuet et al., "Statistical properties of single-mode fiber coupling of satellite-to-ground laser links partially corrected by adaptive optics," *J. Opt. Soc. Amer.*, vol. 35, no. 1, pp. 148–162, 2018.

[18] S. Basu, D. Voelz, and D. K. Borah, "Fade statistics of a ground-to-satellite optical link in the presence of lead-ahead and aperture mismatch," *Appl. Opt.*, vol. 48, no. 7, pp. 1274–1287, 2009.

[19] J.-M. Conan et al., "Adaptive optics for GEO-feeder links: From performance analysis via reciprocity based models to experimental demonstration," in *Proc. Workshop (Commun. Observ. Through Atmospheric Turbulence: Characterization Mitigation)*, Châtillon, France, 2019, pp. 1–10.

[20] D. L. Fried, "Optical resolution through a randomly inhomogeneous medium for very long and very short exposures," *J. Opt. Soc. Amer.,* vol. 56, pp. 1372–1379, 1966.

[21] R. K. Tyson and B. W. Frazier, *Principles of Adaptive Optics*. Boca Raton, FL, USA: CRC Press, 2022.

[22] F. Roddier, *Adaptive Optics in Astronomy*. New York, NY, USA: Cambridge Univ. Press, 1999.

[23] R. J. Noll, "Zernike polynomials and atmospheric turbulence," *J. Opt. Soc. Amer.*, vol. 66, no. 3, pp. 207–211, 1976.

[24] N. Védrenne, J.-M. Conan, C. Petit, and V. Michau, "Adaptive optics for high data rate satellite to ground laser link," *Proc. SPIE*, vol. 9739, pp. 119–128, 2016.

[25] F. Dios, J. A. Rubio, A. Rodríguez, and A. Comerón, "Scintillation and beam-wander analysis in an optical ground station-satellite uplink," *Appl. Opt.*, vol. 43, no. 19, pp. 3866–3873, 2004.

[26] G. J. Baker and R. S. Benson, "Gaussian-beam weak scintillation on ground-to-space paths: Compact descriptions and Rytov-method applicability," *Proc. SPIE*, vol. 44, no. 10, 2005, Art. no. 106002.

[27] J. H. Shapiro, "Reciprocity of the turbulent atmopshere," *J. Opt. Soc. Amer.*, vol. 61, no. 4, pp. 492–495, 1971.

[28] J. H. Shapiro and A. L. Puryear, "Reciprocity-enhanced optical communication through atmospheric turbulence—Part I: Reciprocity proofs and far-field power transfer optimization," *J. Opt. Commun. Netw.*, vol. 4, no. 12, pp. 947–954, 2012.

[29] D. L. Fried, "Anisoplanatism in adaptive optics," *J. Opt. Soc. Amer.*, vol. 72, no. 1, pp. 52–61, 1982.

[30] R. K. Tyson, "Adaptive optics and ground-to-space laser communications," *Appl. Opt.*, vol. 35, no. 19, pp. 3640–3646, 1996.

[31] J. H. Shapiro, "Point-ahead limitation on reciprocity tracking," *J. Opt. Soc. Amer.,* vol. 65, no. 1, pp. 65–68, 1975.

[32] N. Vedrenne et al., "First experimental demonstration of adaptive optics pre-compensation for GEO feeder links in a relevant environment," in *Proc. Int. Conf. Space Opt. Syst. Appl.*, Portland, 2019, pp. 1–5.

[33] N. Leonhard et al., "Real-time adaptive optics testbed to investigate point-ahead angle in pre-compensation of earth-to-GEO optical communication," *Opt. Exp.*, vol. 24, no. 12, pp. 13157–13172, 2016.

[34] O. de Varona, M. Steinke, J. Neumann, and D. Kracht, "All-fiber, single-frequency, and single-mode Er^{3+}:Yb^{3+} fiber amplifier at 1556 nm core-pumped at 1018 nm," *Opt. Lett.*, vol. 43, no. 11, pp. 2632–2635, 2018.

[35] A. Le Kernec et al., "The H2020 VERTIGO project towards tbit/s optical feeder links," *Proc. SPIE*, vol. 11852, 2021, Art. no. 1185217.

[36] J. D. Schmidt, "Propagation through atmospheric turbulence," in *Numerical Simulation of Optical Wave Propagation with Examples in MATLAB*. Washington, USA: SPIE Press,2010, pp. 149–183.

[37] J. Martin and S. M. Flatté, "Intensity images and statistics from numerical simulation of wave propagation in 3-D random media," *Appl. Opt.*, vol. 27, no. 11, pp. 2111–2126, 1988.

[38] N. Védrenne et al., "Turbulence effects on bi-directional ground-to-satellite laser communication systems," in *Proc. Int. Conf. Space Opt. Syst. Appl.*, Corsica, France, 2012, pp. 1–6.

[39] N. Vedrenne et al., "Performance analysis of an adaptive optics based optical feeder link ground station," *Proc. SPIE*, vol. 11852, 2021, Art. no. 1185219.

[40] J. Osborn et al., "Optical turbulence profiling with Stereo-SCIDAR for VLT and ELT," *Monthly Notices Roy. Astronomical Soc.*, vol. 478, no. 1, pp. 825–834, 2018.

[41] D. Sprung and E. Sucher, "Characterization of optical turbulence at the solar observatory at the Mount Teide, Tenerife," *Proc. SPIE*, vol. 8890, pp. 321–329, 2013.

[42] A. Monin and A. Obukhov, "Basic laws of turbulent mixing in the surface layer of the atmosphere," in *Proc. Geophys. Inst., Nat. Acad. Sci., USSR*, 1954, pp. 163–187.

[43] J. L. Bufton, "Comparison of vertical profile turbulence structure with stellar observations," *Appl. Opt.*, vol. 12, no. 8, pp. 1785–1793, 1973.

[44] D. P. Greenwood, "Bandwidth specification for adaptive optics systems," *J. Opt. Soc. Amer.*, vol. 67, no. 3, pp. 390–393, 1977.

[45] K. A. Winick, "Atmospheric turbulence-induced signal fades on optical heterodyne communication links," *Appl. Opt.*, vol. 25, no. 11, pp. 1817–1825, 1986.
[46] S. Shaklan and F. Roddier, "Coupling starlight into single-mode fiber optics," *Appl. Opt.*, vol. 27, no. 11, pp. 2334–2338, 1988.
[47] B. J. Klein and J. J. Degnan, "Optical antenna gain. 1: Transmitting antennas," *Appl. Opt.*, vol. 13, no. 9, pp. 2134–2141, 1974.
[48] L. C. Roberts and W. L. Bradford, "Improved models of upper-level wind for several astronomical observatories," *Opt. Exp.*, vol. 19, no. 2, pp. 820–837, 2011.
[49] *Digital Broadcasting Systems for Television, Sound and Data Services; Framing Structure, Channel Coding and Modulation for 11/12 GHz Satellite Services*, Standard EN 300 421 V1.1.2, ETSI, Sophia Antipolis, France, 1994.
[50] *Digital Video Broadcasting (DVB); Second Generation Framing Strcuture, Channel Coding and Modulation Systems for Broadcasting, Interactive Services, News Gathering and Other Broadband Satellite Applications*, Standard EN 302 307-2 V1.2.1, ETSI, Sophia Antipolis, France, 2020.
[51] E. T. S. I. (ETSI), "Digital video broadcasting (DVB); implementation guidelines for second generation digital terrestrial television broadcasting system (DVB-T2)," ETSI, Sophia Antipolis, France, 2012.
[52] A. T. S. Committee, "ATSC recommended practice: Guidelines for the physical layer protocol (A/327)," ATSC, WA DC, USA, 2018.
[53] G. J. C. Clark and J. B. Cain, *Error-Correction Coding for Digital Communications*. New York, NY, USA: Springer, 1981.
[54] M. A. Islam, M. Y. Arafath, and M. J. Hasan, "Design of DDR4 SDRAM controller," in *Proc. 8th Int. Conf. Elect. Comput. Eng.*, Dhaka, Bangladesh, 2014, pp. 148–151.
[55] J. A. Greco, "Design of the high-speed framing, FEC, and interleaving hardware used in a 5.4km free-space optical communication experiment," *Proc. SPIE*, vol. 7464, 2009, Art. no. 746409.
[56] B. Akesson, *An Introduction to SDRAM and Memory Controllers*. Eindhoven, The Netherlands: Philips, 2017.
[57] *High Bandwidth Memory Dram*, Standard - JESD235D, JEDEC, Solid State Technology, Arlington, VA, USA, 2021.
[58] *DDR3 SDRAM*, Standard - JESD79-3F, JEDEC Solid State Technology Association, Arlington, VA, USA, 2010.
[59] *DDR4 SDRAM*, Standard - JESD79-4D, JEDEC Solid State Technology Association, Arlington, VA, USA, 2020.
[60] *DDR5 SDRAM*, Standard- JESD79-5B, JEDEC Solid State Technology Association, Arlington, VA, USA, 2020.
[61] S. Beppu, K. Kasai, M. Yoshida, and M. Nazakawa, "2048 QAM (66 Gbit/s) single-carrier coherent optical transmission over 150 km with a potential SE of 15.3 bit/s/Hz," *Opt. Exp.*, vol. 23, no. 4, pp. 4960–4969, 2015.
[62] D. Qian, E. Ip, M.-F. Huang, M.-J. Li, and T. Wang, "698.5-Gb/s PDM-2048QAM transmission over 3km multicore fiber," in *Proc. 39th Eur. Conf. Exhib. Opt. Commun.*, 2013, pp. 1–3.
[63] R. Boddeda, S. Almonacil, D. Romero Arrieta, and S. Bigo, "Analog/digital converter requirements for coherent optical satellite communications," in *Proc. Optoelectron. Commun. Conf.*, Toyama, Japan, 2022, pp. 1–3.
[64] I. photonics, 2022. Accessed: Oct. 10, 2022. [Online]. Available: https://www.ipgphotonics.com/en/products/lasers/low-power-cw-fiber-lasers/1-53-1-65-micron/elr-sf-1-30-w

Daniel Romero Arrieta received the M.E. degree in electronic of embedded systems and telecommunications from Paul Sabatier University, Toulouse, France, in 2019. He is currently working toward the Ph.D. degree with Nokia Bell Labs France and the French National Aerospace Research Center, Onera, Paris, France. His research interests include developing a ground-satellite optical communication system, based on coherent detection and adaptive optics technologies, FPGA implementations, digital signal processing, and data interleaving.

Sylvain Almonacil (Member, IEEE), was born in Fontainebleau, France, in 1991. He received the M.Sc. Eng. degree in optics and photonics from Institut d'Optique, Palaiseau, France, in 2016, and the Ph.D. degree in physics from the Paris-Saclay University, Paris, France, in 2019. Since 2016, he has been a Research Engineer with the Optical Systems and Devices Research Lab, Nokia Bell Labs, France. His research interests include digital signal processing for both terrestrial and free-space optical transmissions.

Jean-Marc Conan received the Ph.D. degree from Institut d'Optique Graduate School, France, in 1994. He has been conducting research activities for 30 years in the High Angular Resolution unit of ONERA, the French Aerospace Lab. His research interests mainly include optical propagation through turbulence and adaptive optics, with application to: astronomy, defense, biology, and optical links. He current research focuses on ground space optical links applied to telecoms, quantum key distribution, and frequency dissemination.

Laurie Paillier received the Ph.D. degree from Institut Polytechnique de Paris, Paris, France, in 2020. Her Ph.D. focused on the development of coherent receiver architectures for ground-satellite optical communication links, taking into account the impact of propagation through atmospheric turbulence on the transmitted optical wave. Since 2020, she has been a Research Engineer with the High Angular Resolution unit of ONERA, the French Aerospace Lab. Her research interests include the physics of laser beams focusing in complex media and on the real-time compensation of turbulent effects for telecommunication links in the strong perturbation regime.

Eric Dutisseuil, biography not available at the time of publication.

Sébastien Bigo (Fellow, IEEE) received the graduation degree from the Institut d'Optique Graduate School, France, in 1992. In 1993, he joined Nokia Bell Labs (Alcatel Research & Innovation at the time), while a Ph.D. student with the University of Franche Comté, Besançon, France. After completing the Ph.D. degree in all-optical processing and soliton transmission, he studied high-capacity WDM transmission systems, demonstrating 30 record experiments at 10Gbit/s, 40Gbit/s, 100Gbit/s, and 400Git/s channel rates. His research interests have expanded to automated, dynamic optical networks. He is currently Bell Labs Principal, in charge of optical networking and non-terrestrial networks. He has authored or coauthored more than 380 journal and conference papers, and 50 patents. He has been a Bell Labs Fellow since 2012 and IEEE Fellow since 2017. He was the recipient of the General Ferrié Award in 2003 from the French ICT Society, the IEEE/SEE Brillouin Award in 2008, two Marius Lavet Inventor-Engineer Awards in 2010 and 2017, and the IMT Grand Prize of the Academy of Science of France in 2017.

Jérémie Renaudier (Senior Member, IEEE) received the Ph.D. degree in optical communications from Telecom Paris, Paris, France, in 2006. He joined Bell Laboratories (former Alcatel-Lucent). He primarily worked on the disruptive approach of 100G long-haul coherent systems and contributed to several multiTerabit/s transmission records. Distinguished Member of Technical Staff with Bell Labs since 2014, he has been responsible for forward looking research on coherent systems, including spectrally efficient modulation formats, advanced digital signal processing and coding, Tb/s-class transmissions and ultra-wideband systems. He is currently the Head of the Departments of Optical Transmission Systems and High Speed Analog Devices within the Optical Systems and Devices Research Lab, Nokia Bell Labs. He has authored or coauthored more than 200 articles and holds 35 patents. He is a Technical Program Committee Member of the IEEE European Conference on Optical Communication (ECOC).

Rajiv Boddeda (Member, IEEE) received the master's degree from Ecole Polytechnique, Paris, France, in 2013, and the Doctorate degree from Paris Saclay University, Paris, in 2016. He is currently a Research Scientist with Nokia Bell Labs, working on optical technologies for wireless communications. He worked on the development of optical quantum technologies using cold atoms and photonic circuits. His research interests include digital signal processing, quantum communications, and coherent optical satellite systems.